This paper appears in ASME Journal of Biomechanical Engineering
`https://doi.org/10.1115/1.4048573`

Nine Degree-of-Freedom Kinematic Modelling of the Upper Limb Complex for Constrained Workspace Evaluation

Brayden DeBoon*, **Ryan C. A. Foley**†, **Scott Nokleby***, **Nicholas J. La Delfa**†, **and Carlos Rossa***‡

The design of rehabilitation devices for patients experiencing musculoskeletal disorders (MSDs) requires a great deal of attention. This paper aims to develop a comprehensive model of the upper limb complex to guide the design of robotic rehabilitation devices that prioritize patient safety, while still targeting effective rehabilitative treatment. A 9 degree-of-freedom kinematic model of the upper limb complex is derived to assess the workspace of a constrained arm as an evaluation method of such devices. Through a novel constrained differential inverse kinematic method, the model determines the workspaces in which a patient is able to perform rehabilitative tasks and those regions where the patient needs assistance due to joint range limitations resulting from an MSD. Constraints are imposed on each joint by mapping the joint angles to saturation functions, whose joint-space derivative near the physical limitation angles approaches zero. The model Jacobian is then reevaluated based on the nonlinearly mapped joint angles, providing a means of compensating for redundancy while guaranteeing feasible inverse kinematic solutions. The method is validated in three scenarios with different constraints on the elbow and palm orientations. By measuring the lengths of upper arm segments and the range of motion for each joint, the total workspace of a patient experiencing an upper-limb MSD can be compared to a pre-injured state. This method determines the locations in which a rehabilitation device must provide assistance to facilitate movement within reachable space that is limited by any joint restrictions as a result of MSDs.

1 Introduction

There is a growing need for novel therapeutic techniques focused on the recovery of upper-limb functionality in individuals experiencing musculoskeletal disorders (MSDs) [1]. MSDs typically result from excessive (i.e. chronic or acute) physical loading on tissues and joints. Physical impairment of the motor system, such as in the cases of stroke and cerebral palsy, can also be classified and rehabilitated in a similar manner as many MSDs [2]. These disorders are best characterized by changes in reflex excitability, muscle tone, and restricted range of motion, all leading to difficulties in performing voluntary movements [3, 4]. Approximately only 50% of stroke patients regain full motor function of their upper limbs, suggesting the need for further advancement in upper-limb rehabilitation modalities [1].

Recent advances in robotics have introduced compelling new strategies to enhance recovery from upper-limb disability. Two main paradigms that have been gaining attention are assistive and rehabilitation robotics. One may argue that the ultimate goal of an assistive robot is to fully compensate for disability due to a given pathological condition and improve independence in social settings [5]. These technologies intend to allow individuals to accomplish activities of daily living that would otherwise be difficult or impossible to perform, using for example a manipulator arm [6–9]. With this approach, the patient controls the manipulator using a joystick or force feedback device and may interact with a variety of environments and other individuals via a teleoperation scheme.

Alternatively, one may discern rehabilitation robots as those helping therapists facilitate functional motor recovery of individuals with physical disability [10, 11]. Rehabilitation robots are typically designed for functional training, relearning, and reactivating residual motor function while preventing secondary complications such as muscle atrophy [12]. Although some symptoms of MSDs are permanent, studies have documented positive effects of robotic-assisted functional training in improving motor function of individuals living with cerebral palsy [13] and post-stroke movement impairments [14]. In the case of post-stroke therapy, robot-assisted therapy has demonstrated short-term reduction in motor impairment when compared to conventional rehabilitation therapy, such as muscle activation and speed of movement [15].

Since the symptoms associated with these disorders can vary widely, appropriate treatment must focus on the unique disorders and conditions of each individual [16]. This is

---

*B. DeBoon, S. Nokleby, and C. Rossa, are with the Faculty of Applied Science and Engineering, Ontario Tech University, Oshawa, Canada. E-mail: brayden.deboon@ontariotechu.net; scott.nokleby@ontariotechu.ca; carlos.rossa@ontariotechu.ca.

†R. Foley, and N. La Delfa, are with the Faculty of Health Science, Ontario Tech University, Oshawa, Canada. E-mail: ryan.foley@ontariotechu.ca; nicholas.ladelfa@ontariotechu.ca.

‡Corresponding author.

particularly relevant for robots used in rehabilitation, where quantitative assessment of MSDs is important for evaluating potential effects of treatment [17], guiding the design of a robotic system that complies with the individual's unique needs and motion tolerances [18] and ensuring the individual's safety and comfort during robotic intervention [19]. In particular, a robot that is adaptable to the human limb segment lengths and ranges of motion is crucial. Furthermore, when designing robotic rehabilitation strategies, clinical standards must be considered in order to retain compatibility with traditional therapies while involving minimal robot programming.

From the above discussion, one can infer that in implementing robotic assistance and rehabilitation, assessing the individual's pathological conditions is the very first step. A variety of assessments exist to quantify joint movement ranges. The most common techniques quantify the velocity-dependent response of muscle to passive stretching. One method that has been extensively used clinically involves manually moving a limb through its range of motion and grading the resistance encountered on a five-point ordinal scale [20]. In more sophisticated methods, servo-controlled motors apply controlled displacement or torque to joints while limb angle, torque, and electromyographic responses are recorded [17]. Other measures such as range of motion of each joint achieved with and without assistance, according to the individual's tolerances and level of discomfort, may be included in these assessments.

Based on the identified range of each joint, a kinematic model of the upper limb can be used to identify workspaces where the individual with a disability is able to perform tasks and those regions in which robotic assistance is required. Robotic intervention strategies can then be established based on an individual's specific capabilities. Knowing these workspaces opens up two possibilities. The first possibility concerns assistive and cooperative telerobotics. When an individual interacts with a helper using haptic devices, the teleoperation scheme is often implemented where position control and displacement of one robot is correlated to displacement of the other robot. Since the individual workspace is different from that of the helper, motion may be scaled accordingly by normalizing the devices' positions to their respective workspaces [21]. Thus, tasks outside the patient's reach envelope can be scaled to match their feasible range of motion, allowing both individuals to interact without posing any risk or discomfort to the individual with the disability. The second possibility relates to rehabilitation. It is assumed that the individual is able to move their arm in a given workspace that can be determined through the kinematic model. Robotic assistance is only provided when they are required to move their arm in a region they are not able to reach without assistance.

In this paper, the strategies described above are developed and organized around two main contributions: 1) a 9 degree-of-freedom (DOF) kinematic model of the upper limb is derived to evaluate the individual's range of motion. This is achieved through inverse differential kinematics taking into account the physical limits of each joint. 2) a method to evaluate different workspaces according to unique internal joint constraints, as well as external constraints on the range of motion of the user's hand, while limiting the individual's motion to their feasible range. This is achieved through nonlinear mapping of each joint angle such that the differential inverse kinematics saturates the joint velocities as they approach their respective limits. There are a number of kinematic models for the upper arm with 7-DOF of greater [22–27] however the inverse kinematic solution for the redundant models are usually achieved by reducing the number of evaluated joints to six or less. The proposed inverse kinematic solution finds acceptable values of all nine joints at once within a set of predetermined constraints. To the best of the authors knowledge, this is the first 9-DOF model of the upper limb complex incorporating the joint limits in the formulation of its inverse kinematics. It can be used as an invaluable tool to aid in the design of rehabilitation devices. This paper is organized as follows: Section 2 defines the 9-DOF forward kinematic model of the human upper-limb segment. Section 3 introduces a novel constrained differential inverse kinematic method for evaluation of the task-space redundant model, which is experimentally validated in Section 4.

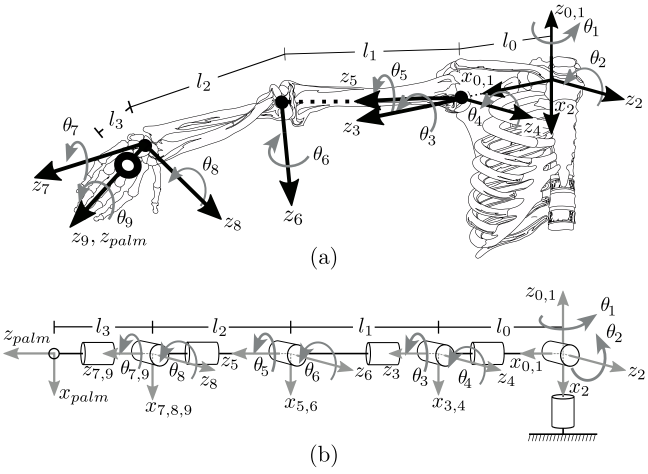

Fig. 1. (a) The equivalent 9-DOF kinematic model overlaid on the upper limb complex. (b) The equivalent zero displacement model of the upper limb complex with the modified Denavit-Hartenberg parameters from Table 1.

2 Forward Kinematics of the Upper Limb

As a first approximation, it is a reasonable assumption to model the mechanical structure of the human arm complex to be composed of 9-DOF. As shown in Fig. 1(a), it is appropriate to schematize the human arm as a quadruple-pendulum whose segments are the clavicle, humerus, forearm, and the hand, connected through the appropriate number of revolute joints [28, 29]. From a kinematic standpoint, it is convenient to single out 2-DOF at the sternoclavicular joint to account for scapular retraction/protraction as well as scapular elevation/depression. In a rehabilitative sense, the scapula is essential to include in the kinematic model for cases in

NOMENCLATURE

$x,\ y,\ z$	Three-dimensional Cartesian coordinates
θ_i	Angle of rotation of joint i about axis z_i
$\mathbf{q} \in \mathbb{R}^{9\times 1}$	Vector of joint space coordinates
$\gamma(q)$	Hand angle w.r.t z_0 (Hand yaw)
$\varphi(q)$	Hand angle w.r.t y_0 (Hand roll)
$\psi(q)$	Hand angle w.r.t x_0 (Hand pitch)
$\mathbf{p} \in \mathbb{R}^{6\times 1}$	Vector of task space coordinates
α_{i-1}	Twist angle between axis z_{i-1}, z_i about x_{i-1}
a_{i-1}	Length of link i along axis x_{i-1}
d_i	Distance from x_{i-1} and x_i about z_i
$\mathbf{T}_i^{i-1}$	Transformation from frame i to frame $i-1$
$\mathbf{T}_i^0 \in \mathbb{R}^{4\times 4}$	Transformation from frame i to base frame
r_{ab}	Element in the a^{th} row and b^{th} column of $\mathbf{T}_i^0$
$\ell_0, \ell_1, \ell_2, \ell_3$	Length of upper limb segments
$\Gamma(q)$	Forward kinematics function
$\dot{q},\ \dot{p}$	Joint space velocities and Cartesian velocity
$\mathbf{J}(q) \in \mathbb{R}^{6\times 9}$	Jacobian matrix $\partial\Gamma(q)/\partial q$
$\theta_i^0,\ \theta_i^u,\ \theta_i^l$	Rest, maximum, and minimum angle of joint i
$\upsilon(\theta),\ \zeta(\upsilon)$	Conversion function of angles and its inverse
$d\zeta \in \mathbb{R}^{9\times 9}$	Weighing matrix of the transformed Jacobian
$\mathbf{J}_c^{\dagger}(\upsilon)$	Damped pseudoinverse transformed Jacobian
$\mu \in \mathbb{R}^+$	Damping coefficient of pseudoinverse Jacobian
$\hat{\mathbf{p}},\ \hat{\upsilon}$	Desired Cartesian trajectory and joint angles
$k_0 \in \mathbb{R}^+$	Inverse kinematics control gain constant

which the shoulder is injured [30]. A 3-DOF spherical joint at the shoulder allows for glenohumeral medial/lateral rotation, glenohumeral adduction and abduction, and humeral flexion/extension, 1-DOF at the elbow allowing for extension and flexion of the forearm and a 3-DOF spherical joint at the wrist, allowing for wrist supination/pronation, flexion/extension, and radial/ulnar deviation. In Fig. 1, ℓ_0 is the acromiohumeral interval, ℓ_1 and ℓ_2 are the lengths of the humerus and forearm, respectively. ℓ_3 is the distance from the distal palmar crease to the wrist crease.

The equivalent kinematic model consisting of nine revolute links is presented in Fig. 1(a). A base frame $x_0y_0z_0$ is fixed at the sternoclavicular joint. Local body frames $x_iy_iz_i$, $i = 1, 2, ...9$, are fixed at the origin of link $i+1$. Frame $i = 10 = palm$ is at the centre of the hand and corresponds to the position of the end-effector. Following the modified Denavit-Hartenberg convention [31], axis i denotes the axis of the joint connecting link $i-1$ to link i. The angle of rotation from x_{i-i} to x_i about the axis z_i is θ_i. Let a_{i-1} be the length of link $i-1$, i.e., the distance between z_{i-1} and z_i axis along x_{i-1} and d_i the joint distance, i.e., the distance between x_{i-1} and x_i along z_i. Let also α_i be the twist angle between axis z_{i-1} and z_i about x_{i-1}. The transformation matrix $\mathbf{T}_i^{i-1}$ from frame i to frame $i-1$ is

$$\mathbf{T}_i^{i-1}(q) = \begin{bmatrix} C\theta_i & -S\theta_i & 0 & a_{i-1} \\ S\theta_i\, C\alpha_{i-1} & C\theta_i\, C\alpha_{i-1} & -S\alpha_{i-1} & -S\alpha_{i-1}d_i \\ S\theta_i\, S\alpha_{i-1} & C\theta_i\, S\alpha_{i-1} & C\alpha_{i-1} & C\alpha_{i-1}d_i \\ 0 & 0 & 0 & 1 \end{bmatrix}, \tag{1}$$

where $\mathbf{q} = [\theta_1\ \theta_2\ ...\ \theta_9]^T \in \mathbb{R}^{9\times 1}$ is the vector of joint variables and S and C represent $\sin(\cdot)$ and $\cos(\cdot)$, respectively. In this section, the subscript of a vector or matrix denotes the frame in which its components are expressed.

The Denavit-Hartenberg parameters for the 9-link mechanism to be used in Equation (1) are summarized in Table 1. It is worth noting that the shoulder and the wrist have spherical joints since all of their respective revolute axes intersect at a single point and thus a_3, a_4, a_5 and a_7, a_8, a_9 equal zero. The centre of rotation of the humerus is shifted from the rotation axis of the scapula joint by ℓ_0 and thus $d_3 = \ell_0$. Likewise, the end-effector is shifted from the centre of rotation of the wrist by ℓ_3 and hence $d_{10} = d_{palm} = \ell_3$. For the 9-DOF mechanism, it follows that the coordinates of a point $\mathbf{c}^j = [x_j\ y_j\ z_j\ 1]^T$ that is expressed in frame j, can be converted to the base frame as:

$$\mathbf{c}^0 = \prod_{i=1}^{j} \left[\mathbf{T}_i^{i-1}(q_i)\right] \mathbf{c}^j = \mathbf{T}_j^0(q)\mathbf{c}^j \tag{2}$$

The x, y, z position of the end-effector in the base frame is

$$[x\ y\ z\ 1]^T = \mathbf{T}_{10}^0(q)[0\ 0\ 0\ 1]^T \tag{3}$$

with $\mathbf{T}_{10}^0 \in \mathbb{R}^{4\times 4}$ being defined in Equation (2). The Cartesian position of the hand as a function of the joint angles is now known. In order to fully specify the pose of the hand, one must also determine its orientation in the base frame.

2.1 Task Space Vector Formulation

Without loss of generality, let $r_{a,b}$ denote the element in the a^{th} row and b^{th} column of the transformation matrix $\mathbf{T}_0^{10}$ defined in Equation (2). The Cartesian position of the palm centre is given by $x(q), y(q)$, and $z(q)$ referenced from the base frame x_0, y_0, z_0, where the x_0 axis is parallel to the line passing through the centre of rotation of both shoulder complexes. The y_0 axis runs perpendicular to the face of the sternum (i.e. in front and behind the individual) and the z_0 axis runs above and below the individual, parallel to a gravity vector. The individual's orientation is defined using Euler angles, specifically by the pitch $\varphi(q)$ of the hand (angle with respect to x_0), its roll $\psi(q)$ (angle with respect to y_0), and its

Table 1. Modified Denavit-Hartenberg parameters for the 9-DOF upper limb complex model.

i	Motion	a_{i-1}	α_{i-1}	d_i	θ_i
1	Scapular retrac./protrac.	0	0	0	θ_1
2	Scapular elev./depr.	0	$-\pi/2$	0	$\theta_2+\frac{\pi}{2}$
3	Shoulder flex./ext.	0	$\pi/2$	l_0	θ_3
4	Shoulder add./abd.	0	$-\pi/2$	0	θ_4
5	Shoulder med./lat. rot.	0	$\pi/2$	l_1	θ_5
6	Elbow flex./ext.	0	$-\pi/2$	0	θ_6
7	Wrist ulnar/radial dev.	0	$\pi/2$	l_2	θ_7
8	Wrist flex./ext.	0	$-\pi/2$	0	θ_8
9	Wrist pron./supin.	0	$\pi/2$	0	θ_9
10	Palm centre transform	0	0	l_3	0

yaw $\gamma(q)$ (angle with respect to z_0), which are given as:

$$\varphi(q) = \tan^{-1}\left(\frac{r_{3,2}}{r_{3,3}}\right), \tag{4}$$

$$\psi(q) = \tan^{-1}\left(-\frac{r_{3,1}}{\sqrt{(r_{3,2})^2+(r_{3,3})^2}}\right), \tag{5}$$

$$\gamma(q) = \tan^{-1}\left(\frac{r_{2,1}}{r_{1,1}}\right), \tag{6}$$

$$x(q) = r_{1,4},\ y(q) = r_{2,4},\ z(q) = r_{3,4}. \tag{7}$$

The task space vector that specifies the hand's position (x,y,z) and orientation (φ,ψ,γ) with respect to the base frame $x_0y_0z_0$ denoted $\mathbf{p} \in \mathbb{R}^{6\times 1}$ can now be defined as $\mathbf{p} = [x\ y\ z\ \varphi\ \psi\ \gamma]^T$.

2.2 Forward Kinematics

The direct kinematics equation specifies the relationship between the joint vector $\mathbf{q}$ and the Cartesian vector $\mathbf{p}$ as

$$\mathbf{p} = \Gamma(\mathbf{q}) \tag{8}$$

Analogously, the relationship between the joint velocities $\dot{\mathbf{q}}$ and Cartesian velocities $\dot{\mathbf{p}}$ is obtained as

$$\dot{\mathbf{p}} = \mathbf{J}(\mathbf{q})\dot{\mathbf{q}} \tag{9}$$

where $\mathbf{J}(\mathbf{q}) \in \mathbb{R}^{6\times 9}$ is the Jacobian matrix $\partial\Gamma(\mathbf{q})/\partial\mathbf{q}$.

It is now clear that the 9-DOF arm is kinematically redundant since the six variables specified in Cartesian space depend each on nine independent joint space variables [32].

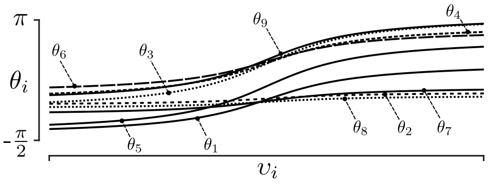

(a) Saturation function of joint angles

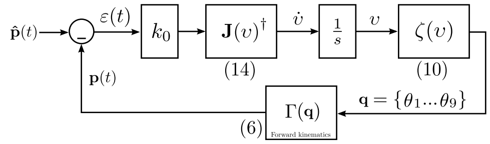

(b) Overview of the constrained differential inverse kinematics

Fig. 2. Overview of the inverse kinematics formulation with joint limits. In (a) each curve shows the transformed joint angle θ_i as a function of the new variable v_i for the joint limits given in Table 1. In (b) the constrained differential kinematics workflow is shown.

3 Constrained Differential Inverse Kinematics

The objective of the constrained differential inverse kinematics is to ensure that the solutions found for each of the nine joint angles for a given end-effector position and orientation fall within the physical limitations of each joint. Instead of discarding potential solutions that do not fall within the limitations of each joint, the purpose of the constrained differential inverse kinematics is to ensure that every solution will meet these requirements. This is accomplished by saturating the joint angle velocities nearing the limits of each joint, similar to natural human motion.

To compute the posture of the upper limb when the hand follows a specific trajectory, the inverse kinematics must guarantee that each joint stays within its physical limits. This can be achieved through a transformation that will bring the joint angles into a new set of variables using a function that saturates a joint angle when it approaches a given limit.

Let θ_i^u and θ_i^l be the upper and lower limits of joint i (see Table 3 for numerical values of an adult individual without disability). The function that transforms the joint variables to the new variables $\upsilon_i = f(q)$ must be continuously increasing in the open interval (θ_i^l, θ_i^u). A suitable candidate for this function is the tangent function $\tan(\theta_i)$, where θ_i is linearly mapped from (θ_i^l, θ_i^u) to $(-\pi/2, \pi/2)$, that is:

$$\upsilon_i(\theta_i) = \tan\left(\frac{\pi}{2}\frac{2\theta_i - \theta_i^u - \theta_i^l}{\theta_i^u - \theta_i^l}\right), \tag{10}$$

and whose inverse

$$\zeta(\upsilon_i) = \theta_i(\upsilon_i) = \frac{\theta_i^u - \theta_i^l}{\pi}\tan^{-1}(\upsilon_i) + \frac{\theta_i^u + \theta_i^l}{2} \tag{11}$$

is bounded to (θ_i^l, θ_i^u) as shown in Fig. 2(a) for the joint limits given in Table 1. This will ensure that the joint limits will not exceed their specified limits in the formulation of the inverse kinematics. Now, one can substitute Equation (11) into the forward kinematics given in Equation (9) and recompute the Jacobian with respect to the new variable $\boldsymbol{\upsilon} = [\upsilon_1 \ \upsilon_2 \ \cdots \ \upsilon_9]^T$. The new Jacobian $\mathbf{J}_c(\boldsymbol{\upsilon})$ is calculated as $\partial\Gamma(\boldsymbol{\upsilon})/\partial\boldsymbol{\upsilon}$, which is equivalent to setting

$$\mathbf{J}_c(\boldsymbol{\upsilon}) = \begin{bmatrix} \frac{\partial x(\boldsymbol{\upsilon})}{\partial \upsilon_1} & \frac{\partial x(\boldsymbol{\upsilon})}{\partial \upsilon_2} & \cdots & \frac{\partial x(\boldsymbol{\upsilon})}{\partial \upsilon_9} \\ \frac{\partial y(\boldsymbol{\upsilon})}{\partial \upsilon_1} & \frac{\partial y(\boldsymbol{\upsilon})}{\partial \upsilon_2} & \cdots & \frac{\partial y(\boldsymbol{\upsilon})}{\partial \upsilon_9} \\ \frac{\partial z(\boldsymbol{\upsilon})}{\partial \upsilon_1} & \frac{\partial y(\boldsymbol{\upsilon})}{\partial \upsilon_2} & \cdots & \frac{\partial y(\boldsymbol{\upsilon})}{\partial \upsilon_9} \\ \frac{\partial \varphi(\boldsymbol{\upsilon})}{\partial \upsilon_1} & \frac{\partial \varphi(\boldsymbol{\upsilon})}{\partial \upsilon_2} & \cdots & \frac{\partial \varphi(\boldsymbol{\upsilon})}{\partial \upsilon_9} \\ \frac{\partial \psi(\boldsymbol{\upsilon})}{\partial \upsilon_1} & \frac{\partial \psi(\boldsymbol{\upsilon})}{\partial \upsilon_2} & \cdots & \frac{\partial \psi(\boldsymbol{\upsilon})}{\partial \upsilon_9} \\ \frac{\partial \gamma(\boldsymbol{\upsilon})}{\partial \upsilon_1} & \frac{\partial \gamma(\boldsymbol{\upsilon})}{\partial \upsilon_2} & \cdots & \frac{\partial \gamma(\boldsymbol{\upsilon})}{\partial \upsilon_9} \end{bmatrix} = \mathbf{J}(\mathbf{q})d\boldsymbol{\zeta}, \tag{12}$$

where the term $d\boldsymbol{\zeta} \in \mathbb{R}^{9\times 9}$ is

$$d\boldsymbol{\zeta} = \begin{bmatrix} \frac{\partial \boldsymbol{\zeta}(\boldsymbol{\upsilon})}{\partial \upsilon_1} & 0 & \cdots & 0 \\ 0 & \frac{\partial \boldsymbol{\zeta}(\boldsymbol{\upsilon})}{\partial \upsilon_2} & \cdots & \vdots \\ \vdots & 0 & \ddots & 0 \\ 0 & \cdots & 0 & \frac{\partial \boldsymbol{\zeta}(\boldsymbol{\upsilon})}{\partial \upsilon_9} \end{bmatrix}. \tag{13}$$

The inverse solution of (9) can now be written considering the change of variables and the saturation of the joint angles as

$$\dot{\boldsymbol{\upsilon}} = \mathbf{J}_c^{\dagger}(\boldsymbol{\upsilon})\dot{\mathbf{p}}, \tag{14}$$

where $\mathbf{J}_c^{\dagger}(\boldsymbol{\upsilon})$ is the damped pseudoinverse of the transformed Jacobian matrix given by

$$\mathbf{J}_c^{\dagger}(\boldsymbol{\upsilon}) = \mathbf{J}_c(\boldsymbol{\upsilon})^T[\mathbf{J}_c(\boldsymbol{\upsilon})\mathbf{J}_c(\boldsymbol{\upsilon})^T + \mu\mathbf{I}]^{-1} \tag{15}$$

if the Jacobian is full rank, providing a least-squares solution with minimum norm to Equation (9). In Equation (15), $\mathbf{I} \in \mathbb{R}^{6\times 6}$ is an identity matrix and $\mu \in \mathbb{R}^+ << 1$ is the damping constant scalar used to avoid possible discontinuity of the pseudoinverse at a singular configuration. In detail, this solution satisfies the condition $\min \|\dot{\boldsymbol{\upsilon}}\|$. Furthermore, provided that $\boldsymbol{\zeta}(\boldsymbol{\upsilon})$ is monotonically increasing in the open interval $(\theta_i^l \ \theta_i^u)$ and given that $\dot{\boldsymbol{\upsilon}} = \dot{f}(\boldsymbol{q})\dot{\boldsymbol{q}}$, the pseudoinverse Jacobian also satisfies $\min \|\dot{\boldsymbol{q}}\|$.

Let $\hat{\boldsymbol{\upsilon}}(t)$ be a solution to $\hat{\boldsymbol{p}}(t) = \Gamma(\boldsymbol{\upsilon})$ relative to a desired Cartesian trajectory $\hat{\boldsymbol{p}}(t) \in \mathbb{R}^{6\times 1}$. A purely proportional control law in the form of

$$\dot{\boldsymbol{\upsilon}} = k_0\mathbf{J}_c^{\dagger}(\boldsymbol{\upsilon})[\hat{\mathbf{p}}(t) - \Gamma(\mathbf{q})], \tag{16}$$

can be shown to ensure that $\boldsymbol{\varepsilon} = \hat{\mathbf{p}}(t) - \Gamma(\mathbf{q}) \to 0$ and then $\boldsymbol{\upsilon} \to \hat{\boldsymbol{\upsilon}}$, provided that $k_0 > 0$. It is important to underscore that $\Gamma(\mathbf{q})$ is the forward kinematics computed with the physical joint angles θ_i calculated through the inverse transformation $\mathbf{q} = \boldsymbol{\zeta}(\boldsymbol{\upsilon})$ using Equation (11). Obviously, the maximum tracking error $\boldsymbol{\varepsilon}$ depends on $\dot{\hat{\mathbf{p}}}$ and inversely on $k_0 \in \mathbb{R}^+$, however, the steady-state error ($\boldsymbol{\varepsilon}$ when $\dot{\hat{\boldsymbol{p}}} = 0$ and $t \to \infty$) is zero [33]. Fig. 2(b) summarizes the closed-loop differential kinematics workflow incorporating the joint limits.

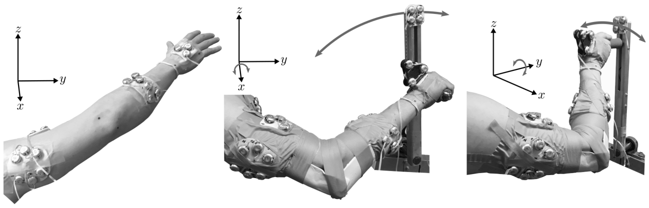

(a) (b) (c)

Fig. 3. Experimental scenarios: (a) Scenario 1: The subject's palm is unconstrained and able to move freely in 3-dimensional space. (b) Scenario 2: The subject is grasping the device that is constrained on a plane normal to the subject's stance. The device constrains the hands translational movement to the $y - z$ plane. The roll rotation $\psi(q)$ of the hand is also constrained. (c) Scenario 3: The subject is grasping the device constrained on a plane parallel to the subject's stance. The device is restricting translational motion to the $x - z$ plane as well as the subjects rotational roll.

Here, four remarks shall be considered before moving forward:

1. Close scrutiny of (15) reveals that $\mathbf{J}_c(\boldsymbol{\upsilon})^{\dagger} = \mathbf{J}(\mathbf{q})^{\dagger}d\boldsymbol{\zeta}^{-1}$ (for $\mu = 0$), meaning that the transformation of variable acts as a gain in the velocity of joints and stiffens those that are close to their limits.
2. The formulation in (16) implies that the arm tends to move from an initial point $\hat{\mathbf{p}}(t = t_0)$ to a new point $\hat{\mathbf{p}}(t = t_1)$ following a trajectory that minimizes the joint velocities. In other words, the hypothesis is that trajectories are chosen to minimize metabolic energy costs, as proved in [34, 35].
3. Because of 2), the trajectory between two points is likely to be a straight line. To accurately represent human behaviour, point-to-point motion must be discretized into several motion primitives.
4. The boundaries of the workspace calculated through the model do not depend on 2) nor 3).

4 Experimental Validation

The constrained workspace evaluation is a method used to determine the reachable workspace of an individual subject to one or more joint limitations. This reduced subset of the reachable workspace can be compared to the workspace of the individual under ideal unconstrained conditions. This evaluation can provide information on locations in Cartesian space under which, for example, a patient may feel discomfort. Three experimental scenarios were conducted to validate the performance of the model. The experimental scenarios are demonstrated in Fig. 3. Scenario 1, shown in Fig. 3(a), evaluated the total reachable workspace of a subject with and without an emulated internal joint constraint. Scenarios 2 and 3, shown in Fig. 3(b) and Fig. 3(c), respectively, demonstrate the total reachable workspace of the subject under additional external constraints of the subject's palm to a predefined trajectory.

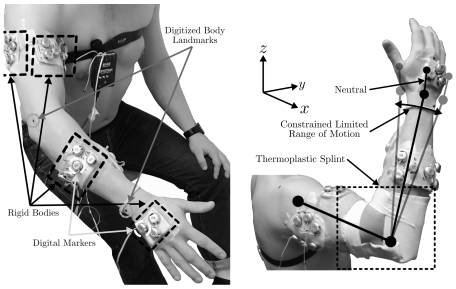

(a) (b)

Fig. 4. (a) Picture of the rigid body setup on an unconstrained subject. This image demonstrates the clusters of rigid bodies used to determine the position and orientation of the limbs of the upper arm complex. Black marks on the body represent points of reference that are calibrated with respect to two or more digital rigid body clusters. (b) Thermoplastic splint limiting the range of motion of the elbow joint approximated by the grey lines.

Table 2. Rigid Body Anatomical Landmarks

Thorax Bodies	Hand Bodies
right acromioclavicular	ulnar styloid process
left acromioclavicular	radial styloid process
right iliac crest	tip of middle finger
left iliac crest	dorsal base, 2nd metacarpal
C7 vertebrae	dorsal base, 5th metacarpal
suprasternal notch	palm centre
xiphoid process	dorsal base, 3rd metacarpal
proximal sacrum	
lateral spine of scapula	

Upper Arm Bodies	Forearm Bodies
right acromioclavicular	medial epicondyle
medial epicondyle	lateral epicondyle
lateral epicondyle	ulnar styloid process
olecranon process	radial styloid process
	olecranon process

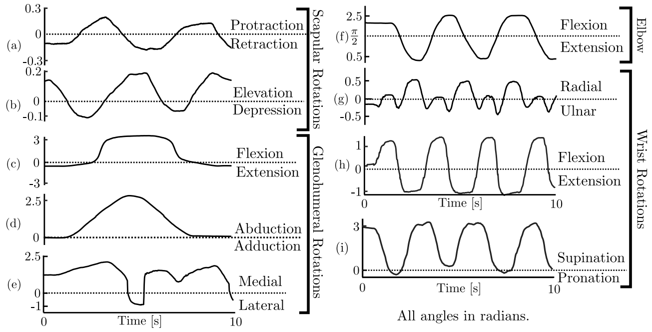

Fig. 5. Unconstrained joint limits. (a) and (b) demonstrate the scapular retraction/protraction and elevation/depression, respectively. (c), (d), and (e) represent the shoulder adduction/abduction, flexion/extension, and medial/lateral rotation, respectively. (f) represents the humeroulnar joint, (g) is the wrist ulnar/radial deviation, (h) is the wrist flexion/extension, and (i) demonstrates wrist pronation and supination. All angles along the vertical axis are shown in radians.

4.1 Data Collection

The model was validated through experimental procedure using an array of Northern Digital Instruments Optotrak 3D Investigator cameras combined with digital markers to provide precise measurements of various points on the upper limb complex as shown in Fig. 4. Three of the cameras were placed along three walls of a room to ensure the digital marker rigid bodies remained within line of sight of at least one of the cameras at all times. The position and orientation of each camera was calibrated to create a global reference frame that is consistent throughout this work and denoted by a coordinate frame in most figures presented hereafter. Once calibration of the cameras was complete, the subject was instrumented with the active digital marker rigid bodies, which are stiff plates used to maintain position and orientation of a small cluster of digital markers. This cluster is then used to calculate the position and orientation of the rigid body. Once the rigid bodies were secured to the subject, various anatomical landmarks were chosen to evaluate the joint angles throughout the experiment. Each landmark which posed a risk of bodily occlusion was instrumented with two or more rigid bodies and, therefore, added redundancy for positional measurements. Table 2 lists the anatomical landmarks and the rigid bodies associated with each landmark. The experiments conducted in this work used at least two rigid bodies on the thorax, two rigid bodies mounted along the humerus, namely the biceps and triceps positions, two rigid bodies mounted along the dorsal and ventral forearm, as well as two rigid bodies attached to the hand. In cases where the virtual landmarks were referenced by two or more rigid body clusters, an optimal Bayesian estimation [36] determined the location of the point used for evaluation.

4.2 Model Identification

As a precursor to the experiments, and to determine the appropriate range of motion for each of the nine aforementioned joint angles, the subject performed a range of exercises tailored to measure the full range of motion of one joint at a time.

Unconstrained scapular joint limits: The first test was to measure the limits of scapular retraction and protraction (θ_1). For this experiment, the subject moved the glenohumeral joint as far in front and behind the coronal plane of the body while attempting to maintain neutral posture. The tests were repeated several times to evaluate the absolute maximum and minimum achievable angles by the subject without external intervention. The results for this test are shown in Fig. 5(a). The next test measured scapular elevation and depression (θ_2) where the subject elevated and depressed the shoulder complex as far as possible while maintaining a stable torso posture in Fig. 5(b).

Unconstrained shoulder complex: Both flexion and extension (θ_3) as well as adduction and abduction (θ_4) were used to evaluate joints 3 and 4. The results are shown in Fig. 5(c) and Fig. 5(d), respectively. Adduction and abduction of the upper arm was evaluated by having the subject stand and elevate the arm from anatomical zero in the $x-z$ (coronal) plane until the maximum height of the palm was reached. Flexion and extension were evaluated in a similar fashion along the $y-z$ (sagittal) plane. Medial and lateral rotation of the glenohumeral joint was measured by abducting the right arm by $\pi/2$ radians and the elbow flexed at $\pi/2$ radians. The subject then attempted internal and external rotation of the forearm while maintaining a static position of the humerus. Results of this experiment for θ_5 are shown in Fig. 5(e).

Unconstrained elbow complex: Fig. 5(f) demonstrates flexion and extension of the elbow (θ_6) which was evaluated by starting at anatomical zero with an outward facing palm and then complete full flexion and extension movements along the sagittal plane.

Unconstrained wrist complex: Fig. 5(g) demonstrates wrist ulnar/radial deviation (θ_7). Fig. 5(h) shows wrist flexion and extension (θ_8), and Fig. 5(i) demonstrates pronation and supination of the wrist (θ_9). The numerical values for the results are shown in Table 3. Note that the numerical values are with respect to the kinematic model described in Section 2.

Table 3. Regular range of motion w.r.t ideal rest angle θ_i^0 (anatomical zero). Angles are in degrees.

	θ_1	θ_2	θ_3	θ_4	θ_5	θ_6	$\boldsymbol{\theta_{6c}}$	θ_7	θ_8	θ_9
θ_i^0	0	0	0	90	0	20	**90**	0	0	0
θ_i^l	-14.1	-6.4	-21.3	0.4	-68.0	15.8	**64.2**	-27.9	-72.1	-5.0
θ_i^u	13.4	12.2	180.0	160.7	133.0	150.5	**114.0**	29.7	81.2	179.4

The subject then donned a thermoplastic brace to the elbow joint to incur a constraint on the individual to demonstrate the validity of the kinematic model as shown in Fig. 4(b). Range of motion tests were done with the constrained joint similar to that of Fig. 5(f) to determine the range of motion for the constrained elbow (θ_{6c}) which was found to be between 1.12 rad (64°) and 1.99 rad (114°). With this information, the model was adapted to fit the newly measured limits using Equation (11). The subject was found to have link lengths of: clavicle = 188 mm, humerus = 286 mm, radius/ulna = 259 mm, and wrist to palm centre = 74 mm. Note that the link lengths correspond to the length between each of the rotational centres of motion and not the length of the bone segments. All values of the joint limits for the range of motion were entered into the simulation model to be used in the assessment of the remaining experiments in this paper. Following the range of motion tests, a series of workspace evaluation experiments were conducted to evaluate the performance of the kinematic model.

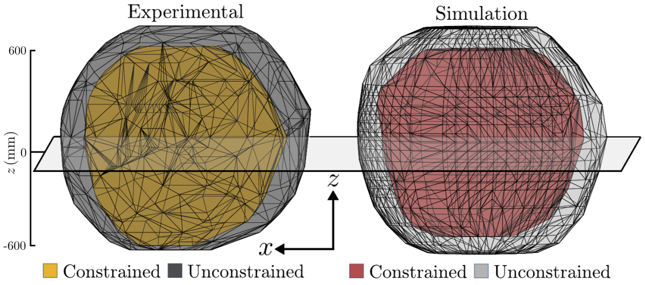

Fig. 6. Experimental and simulated convex hull and slice profile for $z=0$ mm with respect to the subjects sternoclavicular joint. Note that the constrained workspace is a subset of the unconstrained workspace. The 2-dimensional workspace slice profile is shown in Fig. 7

4.3 Scenario 1 Experimental Results

The subject was asked to achieve a reachable workspace by performing a series of movements with an extended arm. Careful precaution was taken to attempt to create a sphere around the subject that best represented the total reachable workspace. The model was compared to the actual reachable workspace of the subject using in vivo motion capture as outlined above. In the first set of experiments, the subject performed the tests to evaluate the total reachable workspace of the individual with no physical limitations to any of the nine joint angles. After this workspace was evaluated, the subject then donned the thermoplastic brace that limited the range of motion of (θ_6) from 0.28 rad to 2.63 rad to (θ_{6c}) which was between 1.12 rad and 1.99 rad. The tests were then duplicated to evaluate the total reachable workspace of the individual under this joint limitation. Convex hull spheres of the resulting experimental and simulated workspaces are shown in Fig. 6. Note that the constrained workspaces are a sub-

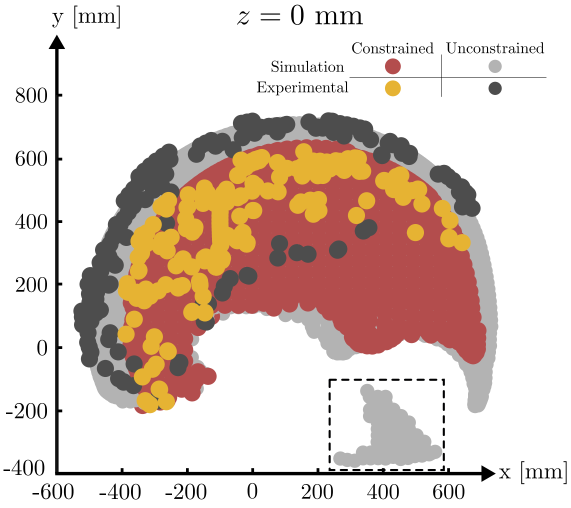

Fig. 7. Slice at $z = 0$ mm in the workspace volume shown in Fig. 6. $z = 0$ mm represents the transverse plane located at the subjects sternoclavicular joint. The locations encapsulated by the dashed box represent reachable locations from an over-the-shoulder topology.

set of the unconstrained workspaces in both the simulated and experimental cases. Fig. 6 also contains a transverse plane situated about the subject's sternoclavicular joint, in which planar images of the workspace can be obtained to better demonstrate the workspaces. Throughout this paper, all Cartesian translations are with respect to a reference frame with its origin centred at the subject's right sternoclavicular joint. The x-axis of this reference frame is along the coronal plane, parallel to the ground. The y-axis of this reference frame is along the sagittal plane, parallel to the ground. The z-axis, centred at the sternoclavicular joint, runs collinear to a gravitational vector, pointing in the direction of the subject's head. A reference frame with this convention is shown in each figure.

Multiple tests were run to collect information on palm locations in Cartesian space under both constrained and unconstrained conditions of the elbow. This was then compared to the simulated model and an overview of the results are shown in Fig. 6. This figure is then extended by demonstrating points of the experimental and simulated workspaces about the transverse slice in in Fig. 7. This slice and other slices in this paper were constructed by considering all measured points within ±10 mm of a transverse plane referenced to the z-axis. In total, 13 slices situated 100 mm apart from one another were evaluated for the experimental and simulated, constrained and unconstrained workspaces. Fig. 8 demonstrates six slices above the sternoclavicular joint, with a final slice at 600 mm above this reference frame. Both the experimental and simulated values are superimposed to demonstrate model accuracy. It is important to note that for these experiments, the total reachable workspace was evaluated and not the total dexterous workspace. That is, the Cartesian position of the end-effector was the only variable to be considered and not the orientation of the palm. The simulated model demonstrates all possible palm locations for all valid arm topologies. For example, the island points in the encased dashed box in Fig. 7 can be physically achieved by an over-the-shoulder topology. The slices shown in Fig. 8 illustrate the achievable regions in which a constrained and unconstrained elbow with the provided joint limitation can physically reach. Note that for slices $z = 100$ mm to $z = 400$ mm, the locations near point (x, y) = (0,0) have cutouts for the subject's head.

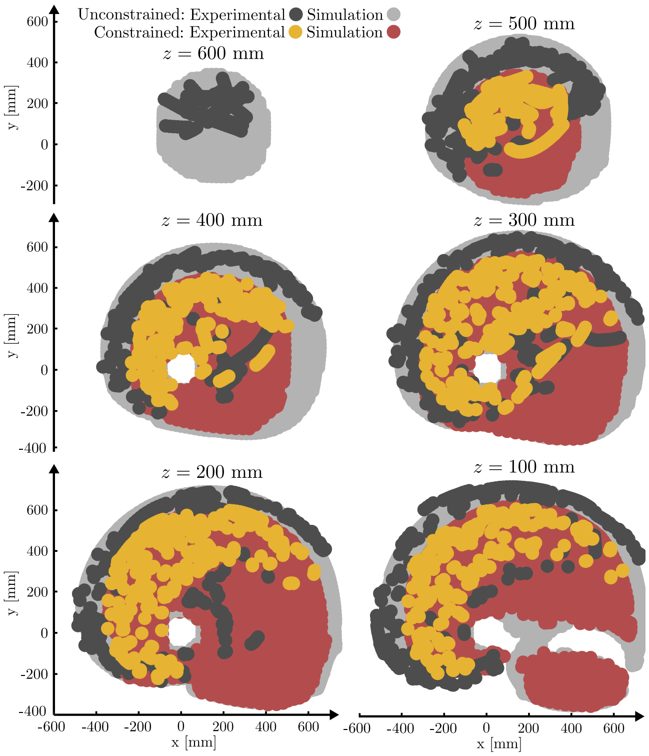

Fig. 8. Experimental and simulated slices of the constrained and unconstrained workspaces along the z axis referenced from the sternoclavicular joint as in Fig. 6. For slices $z = 100$ mm to $z = 400$ mm, cutouts of the subject's neck and head are displayed.

In each of the slices demonstrated by Fig. 8 and Fig. 9, both the experimental and simulated values for the constrained and unconstrained cases compose similar curvatures. As shown, the slices demonstrate that the model can accurately represent experimental data. Similarly for slices under the sternoclavicular reference frame in Fig. 9, cutouts for the subject's torso and lower extremities were provided.

4.4 Scenario 2 Experimental Results

In addition to the emulated internal elbow constraint, two experiments were run to evaluate the workspace of the subject under additional end-effector constraints as well as to measure the joint angles throughout the externally constrained motion. In the first experiment, shown in Fig. 3(b), the subject manipulated a device that constrained the end-effector translation to the sagittal plane. This experiment was conducted at varying radii to validate the performance of the model to evaluate the constrained joint limits. Both scenarios were subject to a new set of constraints, namely the position of the palm (subject to be constrained along the

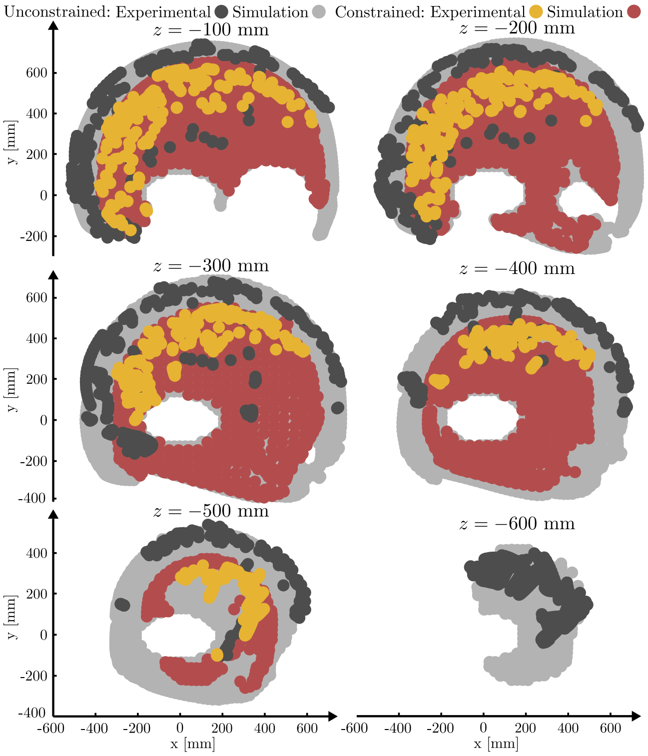

Fig. 9. Experimental and simulated slices of the constrained and unconstrained workspaces along the z axis referenced from the sternoclavicular joint. For slices $z = -100$ mm to $z = -600$ mm, cutouts of the subject's torso and legs are demonstrated.

plane $x = 150$ mm, measured mean $x = 149.80$ mm), and orientation constraints (hand roll = 0 rad) in Equation (4-6):

$$\psi(\mathbf{q}) = 0 \text{ rad} \tag{17}$$

$$x(\mathbf{q}) = 150 \text{ mm} \tag{18}$$

and, therefore, the Jacobian defined in (12) becomes:

$$\mathbf{J}_c(\boldsymbol{\upsilon}) \in \mathbb{R}^{4\times 9} = \begin{bmatrix} \frac{\partial y(\boldsymbol{\upsilon})}{\partial \upsilon_1} & \frac{\partial y(\boldsymbol{\upsilon})}{\partial \upsilon_2} & \cdots & \frac{\partial y(\boldsymbol{\upsilon})}{\partial \upsilon_9} \\ \frac{\partial z(\boldsymbol{\upsilon})}{\partial \upsilon_1} & \frac{\partial y(\boldsymbol{\upsilon})}{\partial \upsilon_2} & \cdots & \frac{\partial y(\boldsymbol{\upsilon})}{\partial \upsilon_9} \\ \frac{\partial \varphi(\boldsymbol{\upsilon})}{\partial \upsilon_1} & \frac{\partial \varphi(\boldsymbol{\upsilon})}{\partial \upsilon_2} & \cdots & \frac{\partial \varphi(\boldsymbol{\upsilon})}{\partial \upsilon_9} \\ \frac{\partial \gamma(\boldsymbol{\upsilon})}{\partial \upsilon_1} & \frac{\partial \gamma(\boldsymbol{\upsilon})}{\partial \upsilon_2} & \cdots & \frac{\partial \gamma(\boldsymbol{\upsilon})}{\partial \upsilon_9} \end{bmatrix} \tag{19}$$

The simulated and measured results are shown in Fig. 10. It is apparent that the model accurately conveys the capabilities of the subject provided with both internal (or simulated internal θ_{6c}) and external constraints (palm fixed along the sagittal plane $x = 150$ mm). Taking this a step further, the behavior of each of the nine kinematic joints throughout the experiments were measured to provide insight on the role of each joint in constraint compensation. This is useful in the context of evaluating joint motions throughout a particular task. Figure 11(a) demonstrates the effect of the movement along the sagittal plane on the unconstrained elbow joint and Fig. 11(b) demonstrates the constrained case. Note that only the internally constrained joint (θ_{6c}) and the constrained end-effector ($\theta_{7,8,9}$) are displayed.

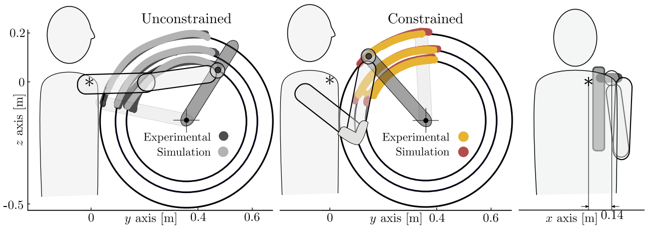

Fig. 10. Results of experimental and simulated workspace evaluation of Scenario 2 at device radii $r = 270$ mm, 330 mm, and 375 mm. Device centred 360 mm in front of sternal notch (y) and 160 mm below sternal notch (z).

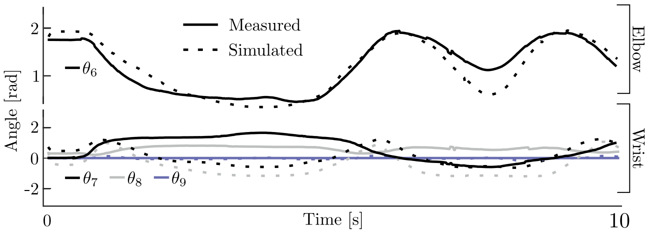

(a) Joint angles with unconstrained elbow

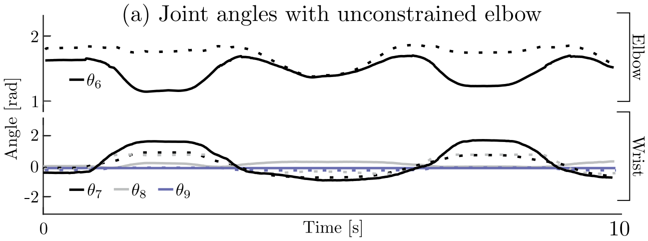

(b) Joint angles with constrained elbow

Fig. 11. Joint trajectory results of Scenario 2. (a) No constraint on the subject's elbow. (b) Subject has donned an elbow brace constraining movement of the elbow. Dashed lines represent the simulation, and solid lines represent experimentally obtained information on the joint angles.

4.5 Scenario 3 Experimental Results

Similar to Scenario 2, Fig. 3(c) demonstrates the third experimental scenario, with constrained translational motion to the $x-z$ (coronal) plane. The subject manipulated the cyclic device in one of three preset radii and a new set of constraints imposed on the subject with the palm constrained along a plane parallel to the coronal plane at $y = 400$ mm, as well as the roll of the wrist, similar to Scenario 2:

$$\psi(\mathbf{q}) = 0 \text{ rad} \tag{20}$$

$$y(\mathbf{q}) = 400 \text{ mm} \tag{21}$$

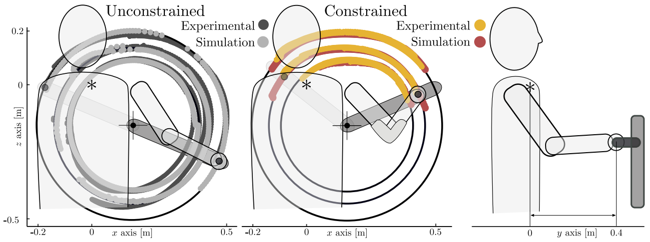

Fig. 12. Results of experimental and simulated workspace evaluation of Scenario 3 at device radii r = 270 mm, 330 mm, and 375 mm. Device centred 160 mm in the x-axis with respect to the sternal notch and 160 mm below sternal notch (z). Device is situated parallel to the coronal plane of the user at $y = 400$ mm.

which results in the following updated Jacobian:

$$\mathbf{J}_c(\boldsymbol{\upsilon}) \in \mathbb{R}^{4\times 9} = \begin{bmatrix} \frac{\partial x(\boldsymbol{\upsilon})}{\partial \upsilon_1} & \frac{\partial x(\boldsymbol{\upsilon})}{\partial \upsilon_2} & \cdots & \frac{\partial x(\boldsymbol{\upsilon})}{\partial \upsilon_9} \\ \frac{\partial z(\boldsymbol{\upsilon})}{\partial \upsilon_1} & \frac{\partial y(\boldsymbol{\upsilon})}{\partial \upsilon_2} & \cdots & \frac{\partial y(\boldsymbol{\upsilon})}{\partial \upsilon_9} \\ \frac{\partial \varphi(\boldsymbol{\upsilon})}{\partial \upsilon_1} & \frac{\partial \varphi(\boldsymbol{\upsilon})}{\partial \upsilon_2} & \cdots & \frac{\partial \varphi(\boldsymbol{\upsilon})}{\partial \upsilon_9} \\ \frac{\partial \gamma(\boldsymbol{\upsilon})}{\partial \upsilon_1} & \frac{\partial \gamma(\boldsymbol{\upsilon})}{\partial \upsilon_2} & \cdots & \frac{\partial \gamma(\boldsymbol{\upsilon})}{\partial \upsilon_9} \end{bmatrix} \tag{22}$$

The results shown in Fig. 12 demonstrate that the model can also determine the feasible workspace while adhering to the constraints provided in this scenario. Additionally, this evaluation method determined the response of each of the nine joint angles with respect to the hand position and orientation. The goal of these experiments was to observe the correlation between the path used and the respective joint angles for a specified trajectory with the simulated model trajectory. Also, with the joint constraints, the subject compensates for the injury by emphasizing movements of the uninjured joints more so than the injured joint. For this cyclic motion task, Fig. 13 shows that the simulated model, even with an elementary cost function, accurately estimates the motion of the constrained and unconstrained joint θ_6. This validates the use of the model in determining joint activation for a particular task, which in turn could be used to tailor rehabilitation tasks to a specific injury as per a professional clinical recommendation.

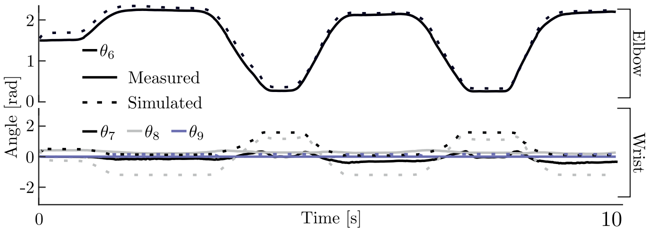

(a) Joint angles with unconstrained elbow

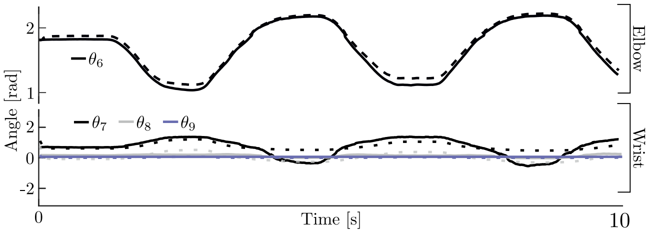

(b) Joint angles with constrained elbow

Fig. 13. Joint trajectory results of Scenario 3. (a) No constraint on the subject's elbow. (b) Subject has donned an elbow brace constraining movement of the elbow. Dashed lines represent simulated data, and solid lines represent experimentally obtained information on the joint angles.

5 Conclusions

The 9-DOF kinematic model of the human upper limb complex derived in this paper accurately demonstrates the workspace envelopes embodied by constrained range of motion. The constrained differential inverse kinematic solution begins with mapping the limitations of each joint to a saturation function. Saturating joint velocities when joint angles approach their limits ensures that the inverse kinematic solution is bounded to the feasible range. Incorporating workspace evaluation using the kinematic model of the upper limb can open up several research avenues. It is well known that the central nervous system selects a pathway by minimizing a given cost function [35, 37]. In the current form, one can clearly see that the trajectory derived from the differential inverse kinematic model is a straight path, which assumes that individuals tend to select a path that minimizes metabolic energy costs [34, 35]. Nevertheless, this is not always the case and it is possible to modify the model in order to select alternative paths that minimize a combination of displacement, velocity, and/or acceleration of specific joints between those points. In future research, this methodology can be combined with strength prediction methods, as a function of hand location and direction [38], to provide a more thorough analysis of the capabilities of the subject.

Optimal trajectory planning based on the kinematic model can also be used to minimize the effects of involuntary joint movements through the forward kinematic model. For instance, the clinician may select a path that minimizes discomfort or highlights subtle movements outside of the constrained workspace to administer rehabilitation. This is equivalent to selecting a position and orientation of the arm less prone to the effects of spasms or discomfort, or by intentionally trying to increase a patient's range of motion. Lastly, as an insight into the structure of an unknown cost function of a specific individual, one may analyze the path followed by the hand through the inverse kinematic model, compute the joint angles, and in doing so may be able to define an approximate cost function to be implemented in robotic rehabilitation and/or assistance.

References

[1] Hochstenbach-Waelen, A., and Seelen, H. A., 2012. "Embracing change: practical and theoretical considerations for successful implementation of technology assisting upper limb training in stroke". *Journal of Neuroengineering and Rehabilitation,* **9**(1), p. 52.

[2] Rios et al., A., 2016. “Playfulness in children with limited motor abilities when using a robot”. *Physical & Occupational Therapy in Pediatrics,* **36**(3), pp. 232–246.

[3] Paneth, N., Hong, T., and Korzeniewski, S., 2006. “The descriptive epidemiology of cerebral palsy”. *Clinics in Perinatology,* **33**(2), pp. 251–267.

[4] Van der Ploeg et al., H., 2004. “Physical activity for people with a disability”. *Sports Medicine,* **34**(10), pp. 639–649.

[5] Maheu et al., V., 2011. “Evaluation of the JACO robotic arm: Clinico-economic study for powered wheelchair users with upper-extremity disabilities”. In International Conference on Rehabilitation Robotics, pp. 1–5.

[6] Graf, B., Hans, A., Kubacki, J., and Schraft, R., 2002. “Robotic home assistant care-o-bot ii”. In Proceedings of the Engineering in Medicine and Biology Conference, Vol. 3, IEEE, pp. 2343–2344.

[7] Kawamura et al., K., 1995. “Intelligent robotic systems in service of the disabled”. *IEEE Transactions on Rehabilitation Engineering,* **3**(1), pp. 14–21.

[8] Najafi, M., Sharifi, M., Adams, K., and Tavakoli, M., 2017. “Robotic assistance for children with cerebral palsy based on learning from tele-cooperative demonstration”. *International Journal of Intelligent Robotics and Applications*, pp. 1–12.

[9] Lum et al., P., 2006. “MIME robotic device for upper-limb neurorehabilitation in subacute stroke subjects: A follow-up study”. *Journal of Rehabilitation Research and Development,* **43**(5), p. 631.

[10] Krebs et al., H., 2004. “Rehabilitation robotics: pilot trial of a spatial extension for MIT-Manus”. *Journal of NeuroEngineering and Rehabilitation,* **1**(1), p. 5.

[11] Mohammadi, E., Zohoor, H., and Khadem, M., 2016. “Design and prototype of an active assistive exoskeletal robot for rehabilitation of elbow and wrist”. *Scientia Iranica. Transaction B, Mechanical Engineering,* **23**(3), p. 998.

[12] Centonze et al., D., 2007. “Repetitive transcranial magnetic stimulation of the motor cortex ameliorates spasticity in multiple sclerosis”. *Neurology,* **68**(13), pp. 1045–1050.

[13] McLaughlin et al., J., 1998. “Selective dorsal rhizotomy: efficacy and safety in an investigator-masked randomized clinical trial”. *Developmental Medicine & Child Neurology,* **40**(4), pp. 220–232.

[14] Lum et al., P., 2002. “Robot-assisted movement training compared with conventional therapy techniques for the rehabilitation of upper-limb motor function after stroke”. *Archives of Physical Medicine and Rehabilitation,* **83**(7), pp. 952–959.

[15] Prange et al., G., 2006. “Systematic review of the effect of robot-aided therapy on recovery of the hemiparetic arm after stroke”. *Journal of Rehabilitation Research and Development,* **43**(2), p. 171.

[16] Dietz, V., and Sinkjaer, T., 2007. “Spastic movement disorder: impaired reflex function and altered muscle mechanics”. *The Lancet Neurology,* **6**(8), pp. 725–733.

[17] Biering-Sørensen, F., Nielsen, J. B., and Klinge, K., 2006. “Spasticity-assessment: a review”. *Spinal Cord,* **44**(12), pp. 708–722.

[18] Veneman et al., J., 2007. “Design and evaluation of the LOPES exoskeleton robot for interactive gait rehabilitation”. *IEEE Transactions on Neural Systems and Rehabilitation Engineering,* **15**(3), pp. 379–386.

[19] Vicentini et al, F., 2014. “Safenet: A methodology for integrating general-purpose unsafe devices in safe-robot rehabilitation systems”. *Computer Methods and Programs in Biomedicine,* **116**(2), pp. 156–168.

[20] Charalambous, C. P., 2014. “Interrater reliability of a modified ashworth scale of muscle spasticity”. In *Classic Papers in Orthopaedics*. Springer, pp. 415–417.

[21] Rossa, C., Najafi, M., Tavakoli, M., and Adams, K., 2017. “Nonlinear workspace mapping for telerobotic assistance of upper limb in patients with severe movement disorders”. In 2017 IEEE International Conference on Systems, Man, and Cybernetics (SMC), IEEE, pp. 2255–2260.

[22] Borbély, B. J., and Szolgay, P., 2017. “Real-time inverse kinematics for the upper limb: a model-algorithm using segment orientations”. *Biomedical Engineering Online,* **16**(1), p. 21.

[23] Wang, K., Li, S., Xu, C., and Yu, N., 2016. “An extended kinematic model for arm rehabilitation training and assessment”. In 2016 International Conference on Advanced Robotics and Mechatronics (ICARM), IEEE, pp. 117–121.

[24] Lioulemes, A., Theofanidis, M., and Makedon, F., 2016. “Quantitative analysis of the human upper-limp kinematic model for robot-based rehabilitation applications”. In 2016 IEEE International Conference on Automation Science and Engineering (CASE), IEEE, pp. 1061–1066.

[25] Barri, M. H., Widyotriatmo, A., et al., 2018. “Path reference generation for upper-limb rehabilitation with kinematic model”. In 2018 IEEE International Conference on Robotics, Biomimetics, and Intelligent Computational Systems (Robionetics), IEEE, pp. 38–43.

[26] Fazel-Rezai, R., Shwedyk, E., and Onyshko, S., 1997. “Three dimensional kinematic model of the upper limb with ten degrees of freedom”. In Proceedings of the 19th Annual International Conference of the IEEE Engineering in Medicine and Biology Society.’Magnificent Milestones and Emerging Opportunities in Medical Engineering’(Cat. No. 97CH36136), Vol. 4, IEEE, pp. 1735–1737.

[27] Masinghe, W., Collier, G., Ordys, A., and Nanayakkara, T., 2012. “A novel approach to determine the inverse kinematics of a human upper limb model with 9 degrees of freedom”. In 2012 IEEE-EMBS Conference on Biomedical Engineering and Sciences, IEEE, pp. 525–530.

[28] Lenarcic, J., and Umek, A., 1994. “Simple model of human arm reachable workspace”. *IEEE Transactions on Systems, Man, and Cybernetics,* **24**(8), Aug, pp. 1239–1246.

[29] Benati et al., M., 1980. "Anthropomorphic robotics". *Biological Cybernetics,* **38**(3), pp. 125–140.

[30] Bolsterlee, B., Veeger, D. H., and Chadwick, E. K., 2013. "Clinical applications of musculoskeletal modelling for the shoulder and upper limb". *Medical & Biological Engineering & Computing,* **51**(9), pp. 953–963.

[31] Hartenberg, R., and Denavit, J., 1955. "A kinematic notation for lower pair mechanisms based on matrices". *Journal of Applied Mechanics,* **77**(2), pp. 215–221.

[32] Xia, Y., and Wang, J., 2001. "A dual neural network for kinematic control of redundant robot manipulators". *IEEE Transactions on Systems, Man, and Cybernetics, Part B (Cybernetics),* **31**(1), Feb, pp. 147–154.

[33] Sciavicco, L., and Siciliano, B., 1988. "A solution algorithm to the inverse kinematic problem for redundant manipulators". *IEEE Journal on Robotics and Automation,* **4**(4), pp. 403–410.

[34] Alexander, R., 1997. "A minimum energy cost hypothesis for human arm trajectories". *Biological Cybernetics,* **76**(2), pp. 97–105.

[35] Ohta et al., K., 2004. "Optimal trajectory formation of constrained human arm reaching movements". *Biological Cybernetics,* **91**(1), pp. 23–36.

[36] Fraser, D., and Potter, J., 1969. "The optimum linear smoother as a combination of two optimum linear filters". *IEEE Transactions on Automatic Control,* **14**(4), pp. 387–390.

[37] Uno, Y., Kawato, M., and Suzuki, R., 1989. "Formation and control of optimal trajectory in human multijoint arm movement". *Biological Cybernetics,* **61**(2), pp. 89–101.

[38] La Delfa, N. J., and Potvin, J. R., 2017. "The arm force field method to predict manual arm strength based on only hand location and force direction". *Applied Ergonomics,* **59**, pp. 410–421.